

Rainbow chains and numerical renormalisation group for accurate chiral conformal spectra

Attila Szabó

Department of Physics, University of Zürich, Zürich, Switzerland

attila.szabo@physik.uzh.ch

Abstract

Based on the relationship between reduced and thermal density matrices in conformal field theory (CFT), we show that the entanglement spectrum of a conformal critical chain with exponentially decaying terms consists of conformal towers of the associated *chiral* CFT, with only weak finite-size effects. Through free-fermion and interacting examples, we show that these entanglement spectra present a reliable method to extract detailed CFT spectra from single wave functions without access to the parent Hamiltonian. We complement our method with a Wilsonian numerical renormalisation group algorithm for solving interacting, exponentially decaying chain Hamiltonians.

Copyright attribution to authors.

This work is a submission to SciPost Physics.

License information to appear upon publication.

Publication information to appear upon publication.

Received Date

Accepted Date

Published Date

Contents

1 Introduction	2
2 Rainbow-deformed chains	3
2.1 Periodic boundary conditions	5
3 Free-fermion examples	5
3.1 Complex fermions (XY chain)	6
3.2 Majorana fermions (critical Ising chain)	8
4 Interacting systems: numerical renormalisation group	9
4.1 Example: the three-state Potts model	11
5 Conclusion	13
A Effective conformal system size	15
References	16

1 Introduction

Over the past decades, studying entanglement properties of quantum many-body states have generated many new insights in condensed-matter theory. In this quest, the notion of the *entanglement spectrum* [1] has proven particularly useful: It is obtained by interpreting the reduced density matrix of a subsystem A as the thermal density matrix of an *entanglement Hamiltonian* $H_{\text{ent},A}$, defined through

$$\rho_A \equiv \exp(-2\pi H_{\text{ent},A}) = \sum_{\alpha} e^{-\lambda_{\alpha}} |\alpha_A\rangle\langle\alpha_A|; \quad H_{\text{ent},A} = \sum_{\alpha} \frac{\lambda_{\alpha}}{2\pi} |\alpha_A\rangle\langle\alpha_A|, \quad (1)$$

where $e^{-\lambda_{\alpha}}$ and $|\alpha_A\rangle$ are the Schmidt values and vectors; the entanglement spectrum is conventionally defined as the set $\{\lambda_{\alpha}\}$. The “low-energy” structure of the entanglement spectrum (that is, the structure of leading Schmidt values) contains fingerprints of exotic physics, which would be challenging to diagnose with conventional tools. For example, the entanglement spectrum of a symmetry-protected topological (SPT) state contains degeneracies that reflect the symmetry group that protect the phase [2, 3], while the entanglement spectrum of two-dimensional fractional quantum Hall [1] and other chiral topologically ordered [4] states reflect the spectrum of the chiral conformal field theories (CFTs) that describe their edge spectra. The latter, combined with momentum-resolved entanglement spectra from MPS [5] or PEPS [6] simulations on finite cylinders, has become the method of choice to pinpoint chiral spin-liquid phases in numerics [7–11].

Remarkably, entanglement spectra of conformally critical one-dimensional chains show the same structure: While these are necessarily achiral [12], their entanglement spectrum matches that of a *boundary* CFT (BCFT) [13–15], whose spectra, like those of chiral CFTs, are generated by a single set of Virasoro generators [16]. This allows us to obtain chiral conformal spectra (albeit without a clear sense of chirality) using purely one-dimensional simulations, as well as study the CFTs underlying one-dimensional critical states, even without access to the parent Hamiltonian.

Extracting detailed information about the underlying chiral CFT is, however, challenging for both of these approaches. In two dimensions, the area law of entanglement entropy [17] limits DMRG simulations to narrow cylinders, on which CFT multiplets quickly broaden and dissolve in a continuum of high-entanglement-energy states. On critical chains of length L , in line with the logarithmic scaling of entanglement entropy [18], finite-size deviations from the expected spectrum scale as powers of $\log L$, requiring simulations on excessively large chains to suppress them.

In this paper, we propose an alternative approach, effectively reversing the relationship between entanglement spectra and BCFTs. Namely, we construct one-dimensional Hamiltonians whose entanglement spectra match those of a BCFT on a segment of length $\sim L$ with uniformly distributed sites, thereby much improving their finite-size scaling. We find that Hamiltonian terms in the bulk of such a chain decay exponentially from its middle, similar to the so-called *rainbow chains* [19–22], which have been proposed as counterexamples to the entanglement area law in one dimension. While the volume-law scaling of entanglement entropy should generally be concerning for MPS simulations, we find that high-quality MPS representations can be built even for long free-fermion chains, allowing us to recover entanglement spectra in much more detail than it would be possible in computationally viable uniform chains.

For interacting theories, we also design a numerical renormalisation-group (NRG) scheme, based on Wilson’s NRG for the Kondo problem [23, 24], to obtain the ground state and low-lying excited states of these rainbow chains, a highly challenging task for variational optimisation methods like DMRG. We obtain these eigenstates in a nonstandard MPS form tailored to their entanglement structure, obviating potential difficulties due to volume-law entanglement.

We also show how to convert this representation to a standard MPS form, thereby obtaining their entanglement spectra, which again recover CFT predictions to excellent accuracy.

We believe that these approaches are applicable to any one-dimensional conformally critical Hamiltonian, as well as CFT wave functions without known parent Hamiltonians. Furthermore, the structure of the NRG flow and fixed points may yield new insights for chiral CFTs and topological orders.

In Sec. 2, we review the connection between CFT entanglement spectra and BCFTs [13,14] and explain our construction of rainbow chains. We demonstrate the power of the approach to obtain accurate spectra for free-fermion CFTs in Sec. 3. We introduce the NRG algorithm in Sec. 4 and demonstrate it for the three-state Potts model in Sec. 4.1. We finish by discussing our results and potential further applications in Sec. 5.

2 Rainbow-deformed chains

While the entanglement Hamiltonian (1) does not necessarily match the Hamiltonian of the system, they are closely related at one-dimensional conformal critical points [14]. The reduced density matrix of the quantum field theory is represented by a path integral with a branch cut across the subsystem in question: For 2D CFTs, the flexibility of 2D conformal transformations often allows this geometry to be mapped onto a rectangle, that is, the thermal density matrix of a finite segment of the CFT. That is, the entanglement Hamiltonian is equivalent to the Hamiltonian of the CFT itself, restricted to a segment, with some boundary conditions. In contrast to CFTs on closed manifolds, the spectrum of such a *boundary CFT* (BCFT) is typically generated by a single set of Virasoro generators, so its conformal blocks match those of the chiral version of the underlying CFT [16].

In the particular case of the ground state of the finite open segment, $\text{Re } z \in (-\pi/4, \pi/4)$, with an entanglement cut at the origin [Fig. 1(a)], such a mapping is given by [14]

$$w = \log \tan z. \quad (2)$$

The mapping must be regularised by excluding a small circle $|z| < r$ from the domain of the path integral; discretising the theory to a chain of L sites automatically achieves this, with a radius $r \sim 1/L$. It follows that the entanglement spectrum matches that of the BCFT on a segment of length $w_0 \approx -\log r \approx \log L$, at inverse temperature $\beta = 2\pi$: this leads to finite-size effects that scale with $\log L$, as observed in Refs. [13,15]. Obtaining detailed and accurate information about the underlying CFT with this method would, therefore, require impractically long chains.

Instead, we propose discretising the continuum CFT to sites that are uniformly distributed *after* the conformal transformation [Fig. 1(b)]. That is, we place lattice sites at $w_n = -n\Delta$ ($n = 0, 1, \dots, L/2 - 1$), or rather, at $z_{\pm n} = \pm \arctan(e^{-n\Delta})$. Based on the discussion above, we expect the entanglement spectrum of the ground state of this system to capture the spectrum of the BCFT on a segment of length $w_1 \sim L\Delta/2$, leading to much more favourable finite-size scaling.

To account for the uneven distribution of sites in the original position space z , we need to use a chain with unequal coupling strengths. In particular, Hamiltonian terms living on bonds have to represent the total Hamiltonian $\int \mathcal{H}(x) dx \approx \mathcal{H}(x_{\text{mid}}) \ell_{\text{bond}}$ on the same bond: While the bond length is proportional to the Jacobian $|dz/dw|$ of the conformal transformation, \mathcal{H} is a component of the stress–energy tensor, and so scales as $|dz/dw|^{-2}$. Therefore, the coupling term as a whole scales inversely proportional to the scale factor:

$$J_i \propto \left. \frac{dw}{dz} \right|_{z=z_i} = \frac{2}{\sin(2z_i)} = 2 \cosh w_i. \quad (3)$$

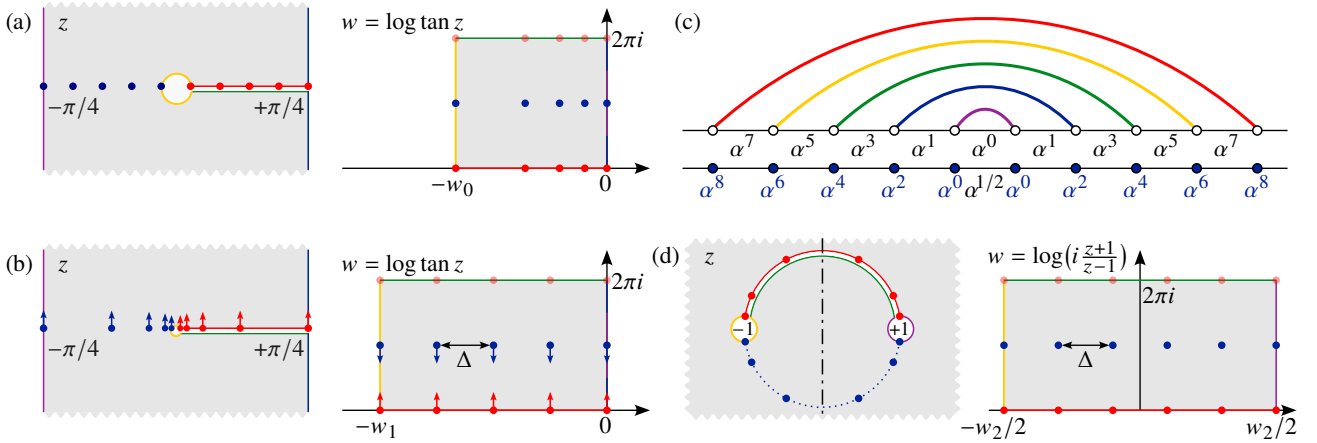


Figure 1: **(a)** The reduced density matrix of an L -site lattice system at a conformal critical point is given by the partition function of the corresponding BCFT on the grey manifold (left). This can be mapped on a BCFT thermal density matrix with system size $w_0 \sim \log L$ using the conformal transformation (2). Therefore, finite-size effects scale with $\log L$, requiring immense system sizes to eliminate them.

(b) If the sites are instead distributed at uniform spacings Δ in the *transformed* space, the entanglement spectrum corresponds to a thermal density matrix at system size $w_1 \sim L$. In the original geometry, this corresponds to non-uniformly spaced lattice sites, which is emulated using position-dependent Hamiltonian terms.

(c) The rainbow chain is a free-fermion tight-binding chain with exponentially decaying couplings (top line): in the limit $\alpha \rightarrow 0$, the ground state is a singlet on each arc of the rainbow, resulting in volume-law entanglement. In models with on-site couplings, the latter also decay exponentially (bottom line). In the limit $w \ll 0$, the conformally deformed chain (b) is identical to a rainbow chain with $\alpha = e^{-\Delta/2}$.

(d) CFT reduced density matrices in periodic boundary conditions can also be mapped onto thermal density matrices, using the conformal transformation (4). (Time runs radially.) The preimage of sites distributed uniformly in w -space between $\pm w_2/2$ remains symmetric under reflection across the imaginary axis. Reflection eigenvalues of Schmidt states can be used to distinguish descendant states with even and odd momentum.

That is, the coupling strength is the highest in the middle of the chain, and decays exponentially towards the edges. We choose to evaluate (5) at the midpoint $w_{i+1/2} = (i + 1/2)\Delta$ of the bond *after* the conformal transformation. In models with both single- and two-site terms, we also scale the former using (3) evaluated at the position of the site.

This prescription, however, does not apply directly to the bond across the entanglement cut, which is not mapped onto the real axis by the conformal mapping. For purely two-site Hamiltonians, we empirically found that evaluating (3) at the position of the last *site* for this bond leads to the best convergence.¹ In the limit of large $w_1 \sim L\Delta/2$, the middle section of the resulting chain matches the *rainbow chain* [19–22] [Fig. 1(c)], a tight-binding chain with exponentially decaying couplings, studied as a counterexample of the area law of entanglement

¹For Hamiltonians with both single- and two-site terms, we obtain the coupling strength of the central bond by evaluating (3) at $-(w_1 + \Delta/4)$. The motivation for this prescription is perhaps the clearest in the Majorana/transverse-field-Ising chain studied in Sec. 3.2. In the Majorana form (8c), all couplings appear to live on “bonds” centred on former bond midpoints as well as sites. The length of these “bonds” is $\Delta/2$, so the left endpoint of the last one would be $\Delta/4$ to the left of the last site. The analogy with the rainbow chain persists, as the full set of coefficients on both bonds and sites still has the same structure, cf. Fig. 1(c).

in local Hamiltonians [17, 25]. In fact, the NRG algorithm in Sec. 4 requires us to use such a chain, with uniform exponential decay all the way to the end, instead of the conformally deformed chain (3); however, this does not appear to change the behaviour of the Hamiltonian significantly.

2.1 Periodic boundary conditions: Reflection symmetry as a proxy for momentum

In addition to open chains, we may also consider conformally critical systems in periodic boundary conditions. These are most naturally represented as a CFT path integral over the whole plane: Imaginary time runs radially, so the reduced density matrix of one half of the ring is obtained using a branch cut along a half-circle [Fig. 1(d)]. This geometry can also be mapped onto a thermal density matrix using the conformal map

$$w = \log\left(i \frac{z+1}{z-1}\right); \quad (4a)$$

on the unit circle $z = e^{i\theta}$ (that is, at imaginary time $\tau = 0$), this reduces to

$$w = -\log \tan \frac{\theta}{2}. \quad (4b)$$

Similar to the case of open boundary conditions, we consider rainbow-deformed rings where the lattice sites are mapped by (4) to w_i at uniform spacing Δ . These can be implemented using coupling terms that scale as

$$J_i \propto \left| \frac{\partial w}{\partial \theta} \right|_{\theta=\theta_i} = \frac{1}{\sin \theta_i} = \cosh w_i, \quad (5)$$

almost identical to (3). We also set the interaction strength on the two bonds at the entanglement cut the same way as explained above.

The key difference between open and periodic boundary conditions is that the post-mapping lattice sites w_i are laid out symmetrically at positive and negative values of w . Even before the mapping, this implies an *exact* mirror symmetry of the Hamiltonian across the imaginary axis, which also requires that all Schmidt vectors be mirror symmetric. Importantly, the symmetry eigenvalue ± 1 can be used to distinguish states that would have even and odd angular momentum in the corresponding chiral CFT: In a BCFT with free boundary conditions, the Virasoro generators L_{-n} are themselves mirror symmetric, with eigenvalue $+1$ (-1) for even (odd) n ; the mirror eigenvalue of a descendant state thus depends on the total parity of Virasoro generators needed to reach it, that is, the parity of its angular momentum.

3 Free-fermion examples

We first illustrate the ideas outlined above through the entanglement spectra of the ground states of quadratic fermionic Hamiltonians. These can be computed using only the spectrum of the single-particle Green's function [26], which can be obtained at modest computational cost even for long chains with coupling strengths spanning several orders of magnitude. Furthermore, as every Schmidt vector of a Slater-determinant (Pfaffian) state is itself a Slater determinant (Pfaffian) [27–30], accurate MPS representations of these wave functions can also be built without the need for computationally expensive variational optimisation (e.g., using DMRG) [30–33].

In particular, we consider the nearest-neighbour tight-binding chain (the closest analogue of the rainbow chain) and the Kitaev chain at the topological transition, the latter of which is equivalent to a nearest-neighbour quadratic Hamiltonian of Majorana fermions. Upon the Jordan–Wigner transformation

$$\sigma_i^+ = (-1)^{\sum^{i-1} n_j} c_i^\dagger; \quad \sigma_i^- = (-1)^{\sum^{i-1} n_j} c_i; \quad \sigma^z = 2c_i^\dagger c_i - 1, \quad (6)$$

these are also equivalent to a nearest-neighbour XY chain and the critical transverse-field Ising (TFI) chain, respectively.

3.1 Complex fermions (XY chain)

We first consider the nearest-neighbour tight-binding chain

$$H = - \sum_i J_{i+1/2} (c_i^\dagger c_{i+1} + c_{i+1}^\dagger c_i) \quad (7a)$$

or, equivalently, the nearest-neighbour ferromagnetic XY chain

$$H = - \sum_i J_{i+1/2} (\sigma_i^+ \sigma_{i+1}^- + \sigma_i^- \sigma_{i+1}^+), \quad (7b)$$

where the hopping terms $J_{i+1/2}$ are given by Eq. (3). For uniform J , such a tight-binding chain is conformally critical, with one left- and one right-moving set of fermionic modes near the Fermi energy. The corresponding BCFT spectrum therefore matches that of *one* copy of the chiral fermion CFT, whose levels are 1, 1, 2, 3, 5, 7, 11, 15, 22, ...-fold degenerate in each charge sector, while the different charge sectors are offset by $(\Delta q)^2/2$, where Δq is the charge deviation from half-filling [34].

We first obtained the ground-state entanglement spectrum of chains of length 256 and 258 with $\Delta = 1/4$, shown in Fig. 2(a,b). As expected, the BCFT spectrum is realised in both cases; the different structure of the two plots is due to half-filling occurring at 64 and 64.5 fermions in each half of the chain, respectively. The conformal spectra are extremely accurate: the multiplicity of even the 11th conformal multiplet can easily be read off from the plot, in sharp contrast to a uniform chain of the same length [Fig. 2(d)], where only the first few levels of the conformal tower can be resolved.

We also computed the entanglement spectrum for the rainbow-deformed ring shown in Fig. 1(d), together with the reflection eigenvalues of the Schmidt states. This is shown in Fig. 2(c): we again obtain very sharp conformal multiplets, which are also distinguished by their alternating reflection eigenvalues in each charge sector, as predicted in Sec. 2.1.

To analyse the dependence of finite-size corrections on the parameters of the chains, we obtained entanglement spectra for a range of system sizes ($10 \leq L\Delta \leq 64$ for $\Delta = 1/2, 1/4, 1/8, 1/16, 1/32$). The length of the chain at fixed Δ has a strong effect on the width of conformal multiplets: they are much more clearly resolved for long chains [Fig. 2(e)]. By contrast, changing Δ even by a factor of 16 at fixed $L\Delta$ has only a modest effect on the entanglement spectrum [Fig. 2(f)]. This two-parameter scaling is shown in more detail in Fig. 2(g) on the example of the mean and standard deviation of the 7th (11-fold degenerate) conformal multiplet. For sufficiently long chains, both of these measures of finite-size effects scale as $1/w^2$, where w is the effective system size after the conformal deformation, labelled $w_{1,2}$ in Fig. 1 (see also Appendix A), with little dependence on Δ . This is consistent with earlier results on the scaling properties of the entanglement spectrum in the rainbow chain [20, 21], as well as the energy spectrum of CFT critical points on a lattice [35]. Similar to these works, we also find that the overall scale of entanglement gaps scales with system size as $1/w$ (not shown), consistent with volume-law scaling of entanglement entropy.

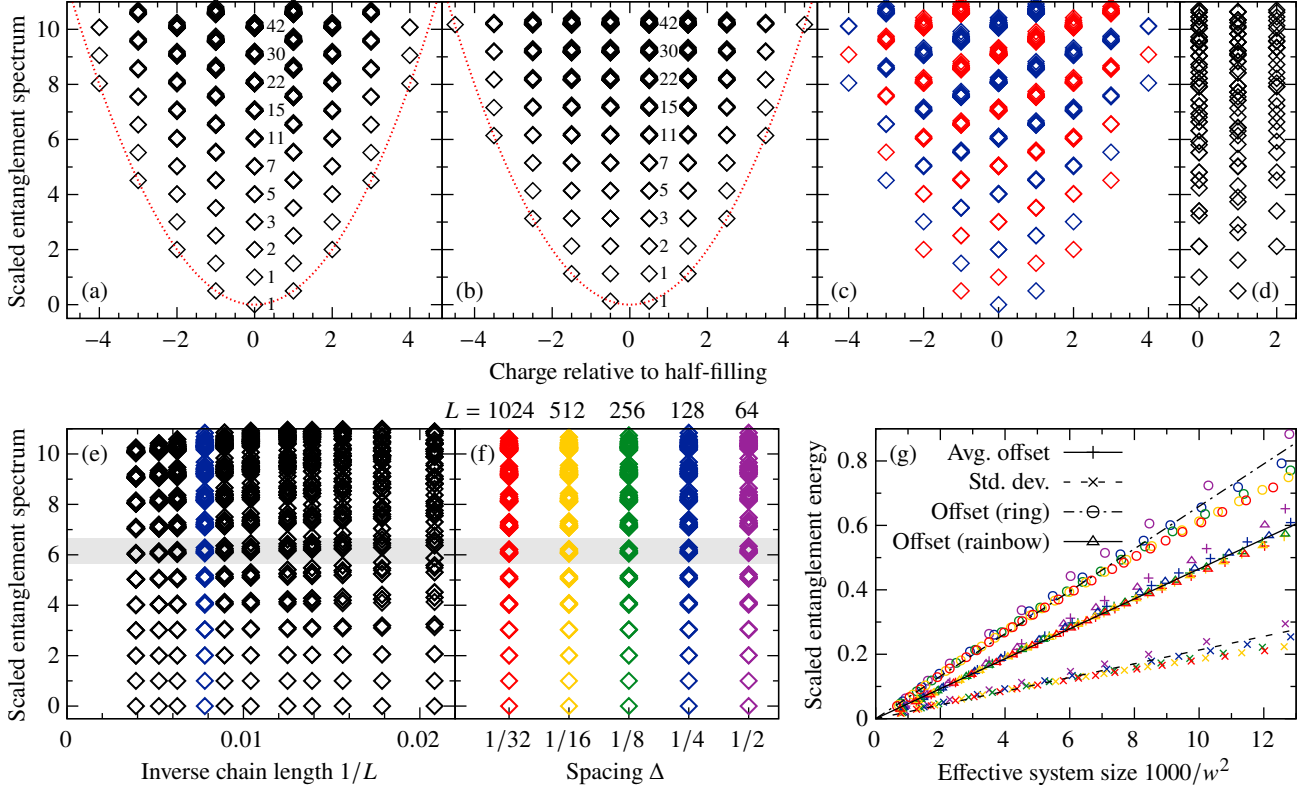


Figure 2: **(a–b)** Ground-state entanglement spectra of the free-fermion chain (7) with the rainbow deformation (3) for $\Delta = 1/4$ and chain length (a) $L = 256$, (b) $L = 258$. Up to 11 degenerate subspaces with the expected multiplicities $1, 1, 2, 3, 5, 7, 11, \dots$ are clearly seen in each charge sector. The red parabolas indicate the expected $(\Delta q)^2/2$ offset of entanglement energy between charge sectors.

(c) Entanglement spectrum of the rainbow-deformed (5) free-fermion ring for $\Delta = 1/4$ and $L = 256$. Colours indicate mirror-symmetry eigenvalues $+1$ (blue) and -1 (red) of the Schmidt vectors, which distinguish subspaces with even and odd momentum.

(d) Part of the ground-state entanglement spectrum of the free-fermion chain with uniform J and $L = 256$. Unlike the rainbow chains, all but the first few CFT multiplets are too far broadened to distinguish.

(e–f) Entanglement spectrum in the half-filled sector for a number of rainbow-deformed chains with (e) fixed $\Delta = 1/4$, (f) fixed $L\Delta = 32$ [highlighted in blue in panel (e)].

(g) Finite-size scaling of the deviation of the $k = 6$ [11-fold degenerate, grey rectangles in panels (e,f)] multiplet as a function of the effective system size w (cf. Appendix A). Both the average distance from the ideal entanglement energy (6 after scaling) and the standard deviation of the multiplet scales as $1/w^2$, with only weak dependence on Δ [indicated by colours, cf. panel (f)]. Straight lines are added as a guide to the eye; to reduce clutter, individual levels are not shown.

All entanglement cuts are at the middle of the chain. The leading entanglement eigenvalue is shifted to $(\Delta q)^2/2 = 0$ or $1/8$, and the first gap within the half-filling charge sector is scaled to 1.

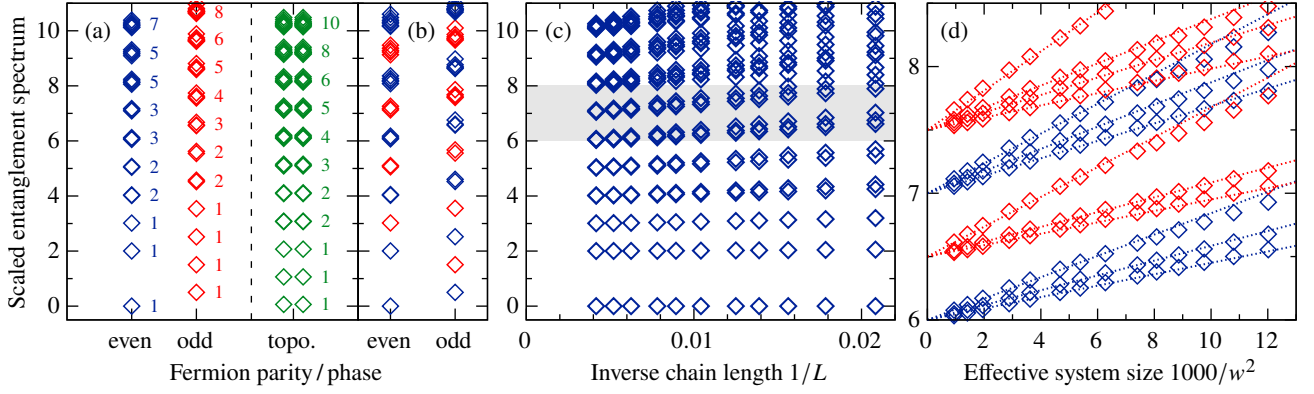


Figure 3: **(a)** Ground-state entanglement spectrum of the rainbow-deformed (3) TFI chain (8) of length $L = 192$ and $\Delta = 1/4$ in the even and odd fermion-parity sectors (blue and red), and after a boundary deformation to induce the SPT phase (green). The multiplicity and spacing of the degenerate subspaces correspond to the identity and fermion sectors of the Ising CFT in the trivial case, and a copy of the twist sector in each parity sector in the topological case.

(b) Entanglement spectrum of the rainbow-deformed (5) TFI ring for $L = 192$ and $\Delta = 1/4$. Colours indicate mirror-symmetry eigenvalues $+1$ (blue) and -1 (red) of the Schmidt vectors, which distinguish subspaces with even and odd momentum.

(c) Entanglement spectrum in the even-parity sector for a number of rainbow-deformed chains with fixed $\Delta = 1/4$.

(d) Finite-size scaling of the $k = 6, 6.5, 7, 7.5$ multiplets on open chains as a function of the effective system size w (cf. Appendix A). The deviation of each level from its expected value is proportional to $1/w^2$ (straight dotted lines as guides to the eye). All entanglement cuts are at the middle of the chain. The leading entanglement eigenvalue is shifted to 0 ($1/16$) and the first gap scaled to $1/2$ (1) in the trivial (topological) chain.

3.2 Majorana fermions (critical Ising chain)

Next, we consider the one-dimensional transverse-field Ising (TFI) chain

$$H = - \sum_i J_{i+1/2} \sigma_i^x \sigma_{i+1}^x + \sum_i h_i \sigma_i^z. \quad (8a)$$

The uniform ($J_i \equiv J$, $h_i \equiv h$) Hamiltonian has a transition between a ferromagnetic and a paramagnetic phase at $J = h$, which is described by the two-dimensional Ising CFT. In the entanglement spectrum of the corresponding rainbow-deformed chains, therefore, we expect to recover conformal towers of the chiral Ising CFT.

To compute the entanglement spectrum of (8a), we map it to a quadratic nearest-neighbour Hamiltonian of Majorana fermions using the Jordan–Wigner transformation (6):

$$H = - \sum_{i=0}^{L-2} J_{i+1/2} (c_i^\dagger - c_i)(c_{i+1}^\dagger + c_{i+1}) + \sum_{i=0}^{L-1} h_i (2c_i^\dagger c_i - 1) \quad (8b)$$

$$= \sum_{i=0}^{2L-1} i t_{i/2} \gamma_i \gamma_{i+1}, \quad (8c)$$

where $t_i = h_i (J_i)$ if i is an integer (half-integer), and we introduce the Majorana operators

$$\gamma_{2i} = c_i^\dagger + c_i, \quad \gamma_{2i+1} = i(c_i^\dagger - c_i). \quad (9)$$

In this Kitaev-chain [36] Hamiltonian, the TFI transition becomes one between a topologically trivial (for $h > J$) and a symmetry-protected topological (SPT, for $h < J$) phase, the latter of which has free Majorana edge modes. We found that wave functions belonging to the topological phase can be induced at the critical point by explicitly decoupling the first and last Majorana modes from the rest of the chain, allowing us to always work with the critical Hamiltonian in the bulk. In variational optimisation methods (e.g., DMRG), similar gossamer perturbations to drive the critical system in specific phases may be introduced by enforcing different on-site symmetries in the MPS [37].

Entanglement spectra of TFI chains with couplings given by (3) are shown in Fig. 3(a) for boundary conditions consistent with both the trivial and the topological phase. In the former case, the entanglement spectrum consists of the conformal towers (0) and (1/2) of the \mathcal{M}_3 minimal model [13], which can be distinguished by the fermion parity of the corresponding Schmidt states [38]. In the topological phase, the entanglement spectrum in both parity sectors is identical and matches the (1/16) conformal tower; the perfect twofold degeneracy of the entanglement spectrum, related to the presence of Majorana edge modes, is a hallmark of an SPT phase [2].

The entanglement spectrum in the rainbow-deformed ring geometry (5) also recovers the $(0) \oplus (1/2)$ conformal towers expected for free boundary conditions [Fig. 3(b)]; as in the complex-fermion case, reflection eigenvalues of the corresponding Schmidt vectors correspond to the parity of the level of the conformal multiplets. Somewhat surprisingly, we were unable to find a deformation of this geometry under which the entanglement spectrum recovers the (1/16) chiral conformal tower.

Similar to the tight-binding model in the previous section, we find that finite-size corrections to the predicted entanglement spectrum scale with the effective system size w (Appendix A) as $1/w^2$, with only weak dependence on Δ [Figs. 3(c, d)].

4 Interacting systems: numerical renormalisation group

We next turn to Hamiltonians that do not admit a free-fermion representation. It would be natural to obtain the ground-state wave function and its entanglement spectrum by variationally optimising an MPS representation using DMRG. However, we found that this algorithm fails to convergence once the dynamical range of coefficients J_i exceeds two or three orders of magnitude; for comparison, the longest chain used in Sec. 3.1 has couplings that differ by a factor of $\approx 5 \times 10^{13}$. We believe that this is mostly due to numerical instability: Minimising the local Hamiltonian on weak-coupling bonds is sensitive to environments that include much stronger Hamiltonian terms, so a tiny improvement on their energy contribution may outweigh optimising the weaker bonds altogether. This effect is exacerbated by the long-range correlations of rainbow chains [cf. Fig. 1(c)].

Instead, we developed a numerical renormalisation-group (NRG) algorithm inspired by Wilson's approach to the Kondo problem [23]. Here, the metallic bath was represented using a semi-infinite tight-binding chain (known as the *Wilson chain*) with exponentially decaying hopping terms, which allows for extracting the low-energy physics by iterative diagonalisation: Lowest-energy eigenstates of the first $(i + 1)$ sites of the chain only have considerable overlap with the lowest-energy eigenstates of the chain of length i , since the relatively weak coupling terms to the last site do not introduce significant perturbations from higher energies. Therefore, the lowest-energy eigenstates at every chain length can be approximated by iteratively diagonalising and restricting the Hamiltonian in the next step onto the lowest few eigenstates. This process can naturally be written as the iterative construction of an MPS representation [Fig. 4(b)] of the lowest eigenstates [39, 40]: The action of the Hamiltonian [represented as a

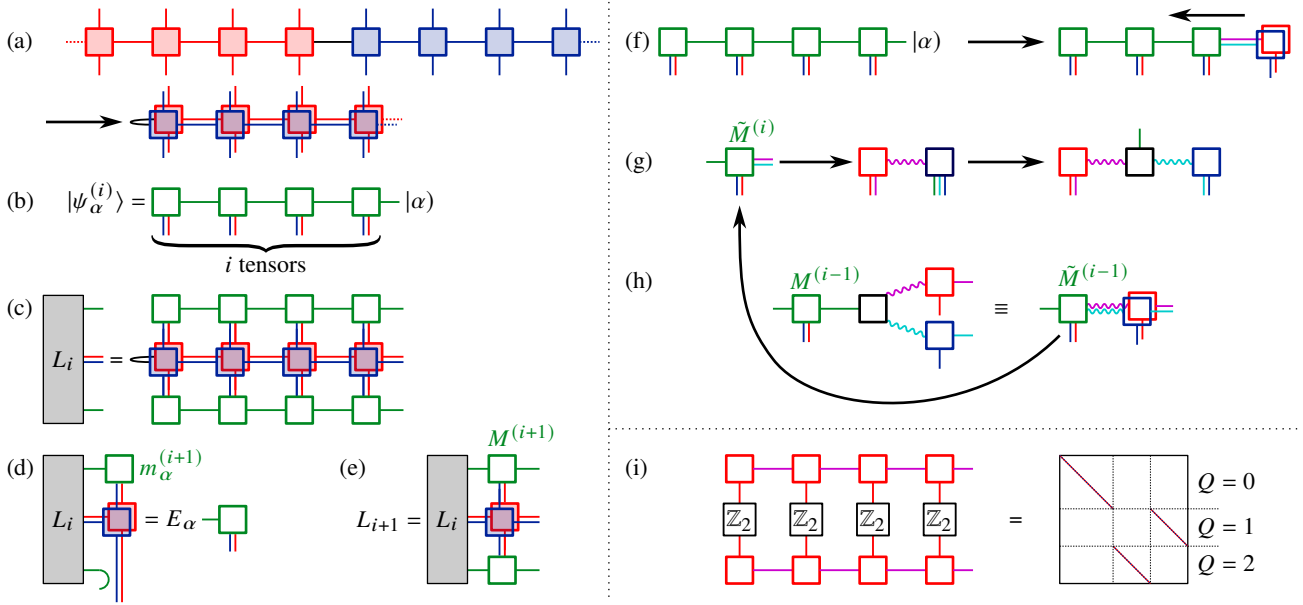


Figure 4: Summary of the numerical renormalisation-group (NRG) algorithm.

The MPO representing the Hamiltonian is folded at the strongest bond of the rainbow chain (a), so that sites with equal interaction strengths on the left and the right can be merged. The low-energy eigenstates of the Hamiltonian are likewise encoded in an MPS with doubled physical legs (b); using these, an environment tensor L_i , capturing the low-energy physics of the middle $2i$ sites of the chain, can be defined (c). The NRG step now consists of diagonalising the effective Hamiltonian (d); the lowest-energy χ_{NRG} eigenvectors build up the new MPS tensor $M^{(i+1)}$, which is used to update the environment tensor (e), now describing a segment of length $2(i+1)$. To obtain the entanglement spectrum and build an MPS wave function with the natural ordering of lattice sites, the resulting MPS must be “unzipped” (f). This is done by splitting isometries involving the left and right physical and virtual legs off $\tilde{M}^{(i)}$ (g) and fusing the remainder into $M^{(i-1)}$ (h), which yields $\tilde{M}^{(i-1)}$ for the next step. (i) Schmidt states of the three-state Potts model with trivial \mathbb{Z}_3 charge are eigenstates of the \mathbb{Z}_2 parity operator with eigenvalue ± 1 , distinguishing the 0^\pm irreps of S_3 ; the other two charge sectors map onto each other.

matrix-product operator (MPO)] on the lowest eigenstates of a chain of length i can be compressed into an environment tensor [Fig. 4(c)], which yields the effective Hamiltonian for step $(i+1)$ [Fig. 4(d)]; the new MPS tensor is made up of the lowest-energy eigenvectors of this effective Hamiltonian, which (after scaling the MPO to counteract the exponential decay of Hamiltonian terms) also gives the new environment tensor for $(i+1)$ sites [Fig. 4(e)].

This NRG protocol is popular for solving the Kondo problem and the Anderson impurity problem in dynamical mean-field theory [24], but has seen little use outside of this context. However, it is a convenient choice for solving rainbow chains, whose Hamiltonian terms also decay exponentially: The approximation of iterative diagonalisation and discarding high-energy states remains valid, even if the Hamiltonian is not a free-fermion one. Furthermore, as the rainbow chain represents a critical phase, we expect the NRG procedure to flow towards a fixed point, which can readily be verified numerically.

The only change to the algorithm outlined above is that the Hamiltonian terms of equal strength on the two sides of the chain must be handled simultaneously, requiring us to fold

Label	dimension	\mathbb{Z}_3	\mathbb{Z}_2
0^+	1	0	+
0^-	1	0	-
E	2	$1 \oplus 2$	$+ \oplus -$

Table 1: Irreducible representations (irreps) of the S_3 on-site symmetry group of the three-state Potts model and their decompositions into irreps of the \mathbb{Z}_3 subgroup preserved by \hat{Z} and the \mathbb{Z}_2 subgroup preserved by $\hat{X} + \hat{X}^\dagger$, labelled respectively with a \mathbb{Z}_3 charge and a parity.

the MPO Hamiltonian at the central bond of the rainbow chain [Fig. 4(a)].² Accordingly, the low-energy states are represented by MPS whose tensors have *two* physical legs, each corresponding to a site in the left and right halves of the chain, respectively [Fig. 4(b)]. This in fact matches the entanglement structure of the expected rainbow ground state, which, in the limit $\alpha \rightarrow 0$, consists of singlet dimers precisely between the fused sites: such a state can be represented as an ‘‘MPS’’ of bond dimension 1. More generally, the folded representation naturally allows for volume-law entanglement, since the left and right halves of the chain are not coupled through a single MPS bond, but rather by *all the tensors*. This means that, in principle, we can obtain the ground state of a rainbow chain of arbitrary length and dynamical range of parameters, even outperforming the free-fermion method, which relies on numerically diagonalising the full single-particle Hamiltonian.

However, extracting the entanglement spectrum from such a representation is not straightforward, requiring us to reconstruct a standard MPS form of the ground state (or a low-lying excited state). We do so using the ‘‘unzipping’’ algorithm shown in Fig. 4(f-h): Starting from the outer end of the MPS returned by NRG, we iteratively split isometries involving the left and right pairs of virtual³ and physical legs, and fuse the remainder into the next tensor. This can be done using either QR or singular-value decompositions; we prefer the latter, as it gives a more controlled way to truncate the decomposition to a fixed bond dimension. The end result is a mixed canonical MPS representation with orthogonality centre on the central bond, so the entanglement spectrum can directly be read off.

4.1 Example: the three-state Potts model

We demonstrate the algorithms outlined above on the ferromagnetic three-state Potts model

$$H = - \sum_{i=1}^{L-1} J_{i+1/2} (X_i X_{i+1}^\dagger + X_i^\dagger X_{i+1}) - \sum_{i=1}^L h_i (Z_i + Z_i^\dagger) - h_L (X_1 + X_1^\dagger) - h_R (X_L + X_L^\dagger), \quad (10)$$

where X and Z are 3×3 matrices acting on each site, satisfying $XZ = \omega ZX$ ($\omega = e^{2\pi i/3}$ is the third root of unity), e.g.,

$$X = \begin{pmatrix} 1 & 0 & 0 \\ 0 & \omega & 0 \\ 0 & 0 & \omega^2 \end{pmatrix}, \quad Z = \begin{pmatrix} 0 & 1 & 0 \\ 0 & 0 & 1 \\ 1 & 0 & 0 \end{pmatrix}. \quad (11)$$

In the absence of the boundary fields $h_{L,R}$, Eq. (10) is symmetric under simultaneous permutations of the basis states in (11) on all sites. These on-site symmetries form a non-Abelian S_3

²This approach is identical to the standard NRG treatment of spinful baths, represented by two Wilson chains that only interact via the impurity site [23].

³At the outermost tensor, virtual legs can either be omitted or trivial ones added for convenience.

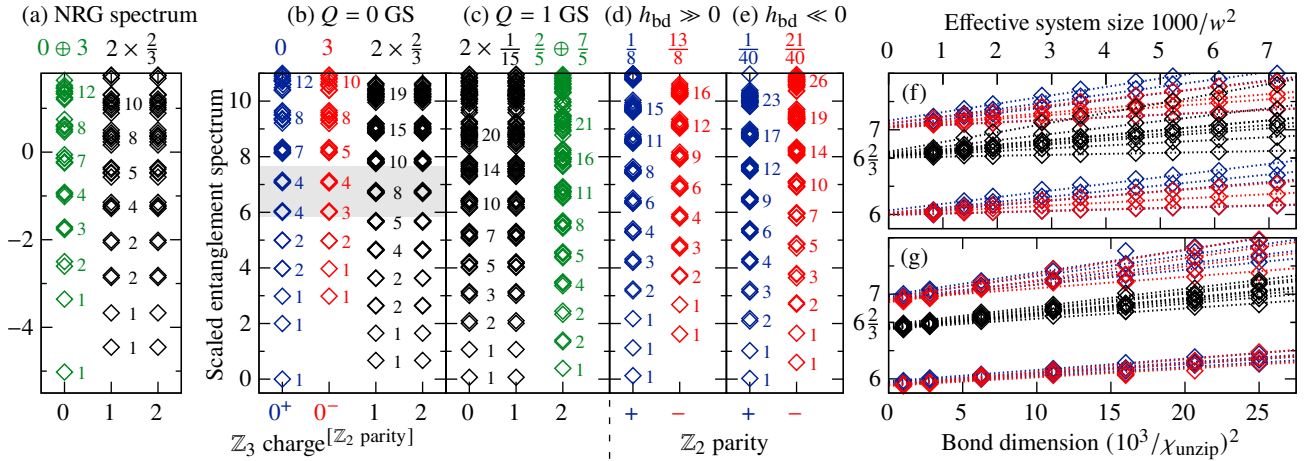


Figure 5: **(a)** Low-energy spectrum of the ferromagnetic critical 3-state Potts model on a rainbow chain, obtained from the numerical renormalisation group (NRG).

(b–c) Entanglement spectrum of the lowest-energy state of the rainbow chain in the ground state **(b)** and the first excited state in symmetry sector E **(c)**. Schmidt vectors are labelled with their eigenvalue under $\mathbb{Z}_3 < S_3$, as well as their \mathbb{Z}_2 parity where that symmetry is preserved.

(d–e) Entanglement spectrum of the ground state upon applying strong positive **(d)** and negative **(e)** boundary fields h_L, h_R . Schmidt vectors are labelled with their parity under the $\mathbb{Z}_2 < S_3$ symmetry preserved by the boundary fields.

The number next to each CFT multiplet indicates its multiplicity; the numbers above each spectrum identify the corresponding conformal tower of the \mathcal{M}_5 minimal model. **(f–g)** Scaling of the $k = 6, 6 + 2/3, 7$ multiplets of the ground-state entanglement spectrum [grey rectangle in **(b)**] as a function of effective system size w for a range of chain lengths L **(f)** and of χ_{unzip} **(g)**. Finite-size effects scale as $1/\chi_{\text{unzip}}^2$ and $1/w^2$ (dotted straight lines fitted to the data).

Unless otherwise stated, all simulations use $L = 256, \Delta = 1/4, \chi_{\text{NRG}} = \chi_{\text{unzip}} = 400$. Entanglement spectra are scaled by the first gap in the leading symmetry sector, and the lowest level is shifted to match the CFT prediction.

group: eigenstates and entanglement spectra can be labelled with irreducible representations (irreps) of this group, which are listed in Table 1. In numerical simulations with TeNPy [41], we enforced the largest Abelian subgroup of S_3 , the \mathbb{Z}_3 group of cyclic permutations. Irreps of this group are labelled by eigenvalues of Z , so the Hamiltonian can be written in the irrep basis by swapping the definitions of X and Z in (11). The boundary fields $h_{L,R}$, on the other hand, break the \mathbb{Z}_3 symmetry, leaving only the $\mathbb{Z}_2 < S_3$ group generated by swapping the ω, ω^2 eigenvalues of X (or, in fact, of Z). The correspondence between the irreps of S_3 and of these groups is also listed in Table 1.

The uniform (that is, $J_i \equiv J, h_i \equiv h$) Potts model has a self-dual critical point at $J = h$, described by the \mathcal{M}_5 conformal minimal model [42]. In analogy with the critical TFIM in Sec. 3.2, we therefore construct a rainbow chain with exponentially decaying couplings in the pattern shown in Fig. 1(c) (for easy comparison, we keep the parameter Δ , defined through $\alpha = e^{-\Delta/2}$). We indeed find that for sufficiently high Δ and a sufficiently large number χ_{NRG} of low-energy states kept, the NRG procedure converges to a fixed-point spectrum. This spectrum is shown in Fig. 5(a): In line with theoretical predictions for the three-state Potts CFT with free boundaries [16, 38], the spectrum consists of the conformal towers $(0) \oplus (3)$ (in the 0^\pm irreps of S_3) and two copies of the tower $(2/3)$ (in the two-dimensional E irrep).

We next obtained the entanglement spectrum of the ground state using the unzipping algorithm in Fig. 4(f–h) [Fig. 5(b)]: we find the same structure as in the energy spectrum, as expected. Since the ground state is symmetric under the full S_3 group, the irreps 0^+ and 0^- can also be distinguished by computing the eigenvalues of the Schmidt vectors under the \mathbb{Z}_2 group generator, as shown in Fig. 4(i). We find that the (0) and (3) conformal towers appear in separate irreps: This is a remarkable difference to the partition function of the boundaryless three-state Potts model [43, 44], where these two conformal towers are bound together by offdiagonal terms.

We also computed the entanglement spectrum of the lowest-energy state in the \mathbb{Z}_3 symmetry sector $Q = 1$, shown in Fig. 5(c). This spectrum contains the conformal towers $(2/5) \oplus (7/5)$ ($Q = 2$ sector) and two copies of the tower $(1/15)$ ($Q = 0, 1$ sectors): this is surprising, as these towers do not appear in the BCFT energy spectrum for free boundary conditions [38], but rather for certain fixed ones [16].

In fact, entanglement spectra of states in nontrivial symmetry sectors do not map straightforwardly on a BCFT spectrum. Under the conformal transformation (2), the “ket” Hilbert spaces of the two halves of the rainbow-deformed chain in Fig. 1(b) map onto a “ket” Hilbert space at $\text{Im } w = 0$ and a “bra” Hilbert space at $\text{Im } w = \pi$, respectively (cf. arrows in the figure). If these are related to one another by imaginary time evolution under a symmetric Hamiltonian, the symmetry quantum numbers of the “ket” Hilbert spaces must match; that is, the original chain must have trivial symmetry quantum numbers. Other entanglement spectra correspond to BCFT spectra with “twisted boundary conditions” in imaginary time, where symmetry quantum numbers change from $\text{Im } w = 0$ to π , then revert to their original values by 2π . In future work, it will be interesting to understand the mechanism that gives rise to CFT spectra in such a setup, including predictions for the conformal towers that can be obtained this way.

Finally, we consider the ground-state entanglement spectrum of (10) in the presence of strong boundary fields $h_{L,R}$. Upon the conformal mapping (2), this corresponds to a finite-temperature BCFT with free boundary conditions on the side of the entanglement cut (where the Hamiltonian was not changed) and fixed ones on the other side. The spectrum for this setup was predicted [16, 38] to contain the conformal towers $(1/8) \oplus (13/8)$ and $(1/40) \oplus (21/40)$ in the limit of strong positive (negative) boundary fields, even though these do not appear in the spectrum of the boundaryless critical Potts model [43, 44]. We indeed recover these in our simulations, see Fig. 5(d,e); the two conformal towers are readily distinguished by their \mathbb{Z}_2 symmetry eigenvalues.

The deviation of entanglement energies from their thermodynamic-limit value scales with the effective system size w as $1/w^2$, similar to the free-fermion systems in Sec. 3 [Fig. 5(f)]. This indicates that MPS with modest bond dimensions are able to accurately represent the leading Schmidt states even for these large systems, without limitations of a finite correlation length. Empirically, we find that the deviation depends on the MPS bond dimension χ in this limit as $1/\chi^2$ [Fig. 5(g)].

5 Conclusion

In this work, we have developed a method to obtain detailed spectral information about conformal field theories using entanglement spectra. By exploiting the conformal mapping between reduced and thermal density matrices [14], we designed chain Hamiltonians whose entanglement spectra match the energy spectrum of long conformal chains, thereby removing the obstacle of logarithmic finite-size scaling [13, 15]. The interaction terms in the bulk of such a chain decay exponentially, similar to the so-called rainbow chains [19–22]. We first demon-

strated our method on free-fermion Hamiltonians, where we could obtain entanglement spectra from single-particle calculations [26]. Indeed, we found that entanglement spectra match those of the expected chiral free-fermion and Ising CFTs, with up to 11 levels of the conformal tower clearly resolved in each symmetry sector: This is a significant improvement over uniform chains and the edge spectra of narrow cylinders, where the entanglement conformal spectra can often only resolve the first few states.

We also proposed a Wilsonian numerical renormalisation group (NRG) algorithm for obtaining low-energy eigenstates for rainbow chains that represent interacting (non-free-fermion) Hamiltonians. In contrast to earlier work [39], we find that this algorithm clearly outperforms such alternatives as DMRG on the problem at hand; most importantly, it can handle chains with an arbitrarily wide dynamical range of Hamiltonian terms, as they are optimised hierarchically. Furthermore, the wave function is returned as a folded MPS [Fig. 4(b)], which is well-suited to the volume-law entanglement structure of the rainbow ground state. We benchmarked the NRG algorithm on the three-state Potts model: By computing ground- and excited-state entanglement spectra in different boundary conditions, we were able to obtain the spectrum of every conformal tower of the chiral \mathcal{M}_5 minimal model with excellent accuracy and level of detail.

As it makes no strong assumptions about the structure of the underlying Hamiltonian, our NRG approach is in principle applicable to any conformal quantum critical point in $(1 + 1)$ dimensions. This will allow us to identify the underlying CFTs through access to their full spectra rather than only, e.g., their central charge. For such applications, it will be important to understand the structure of the NRG flow near the critical point so it can be distinguished from the fixed points corresponding to the surrounding phases.

The structure of the NRG fixed-point tensor itself will also be an interesting target for exploration, as it provides a compact representation of *every* conformal tower of the underlying CFT. Indeed, these can all be extracted from the same MPS, with tensors converging to the fixed-point one, by changing only the final tensor as boundary conditions are changed (cf. Fig. 5). Furthermore, the NRG procedure has a clear sense of directionality, so an MPS made of fixed-point tensors with periodic boundary conditions may well encode the density matrix of a genuinely chiral CFT, similar to the boundary MPS that represent the reduced density matrix of a two-dimensional PEPS state [6]. Comparing these two approaches to obtain approximate MPS representations of chiral conformal spectra may also provide new insights into the representability of chiral topological order with PEPS [11].

Even more importantly, computing entanglement spectra only requires wave functions, not necessarily Hamiltonians, at the critical point. This will allow us to analyse critical wave functions obtained by other means and extract its underlying CFT or even parent Hamiltonian. This is a particularly promising feature for capturing edge theories of topological states (e.g., chiral spin liquids) constructed through a parton construction. Topological transitions between such phases would normally be detected through entanglement properties [45–47]; we expect that detailed access to the evolution of the entanglement spectrum across the transition will yield new insights into their mechanism.

Acknowledgements

I thank Natalia Chepiga, Juraj Hasik, Titus Neupert, and Hong-Hao Tu for helpful discussions. I am especially grateful to Andreas Läuchli for pointing out the similarity between rainbow chains and Wilson chains. MPS calculations were performed using the TeNPy library [41].

Δ	chain (3)	rainbow chain	ring (5)
1/64	4.8364	5.0858	8.3021
1/32	4.1276	4.3848	6.9002
1/16	3.4032	3.6759	5.4827
1/8	2.6476	2.9510	4.0339
1/4	1.8294	2.1934	2.5226
1/2	0.8863	1.3675	0.8863

Table 2: Deviation of conformal chain length $w_{1,2}$ from $L\Delta/2$ for the three types of deformed chain and the values of Δ considered in this work in the limit of $L\Delta \gg 1$.

Funding information A. Sz. was supported by the Ambizione grant No. 215979 by the Swiss National Science Foundation.

A Effective conformal system size

In the first approximation, the conformal transformations (2, 4) map reduced density matrices of the rainbow-deformed chains/rings to the thermal density matrix of a system of size $(L/2 - 1)\Delta$ (cf. Fig. 1). This picture, however, is not completely accurate for the chains we really use in the simulations, mostly because the effective size of the segment of the chain across the entanglement cut is scaled by a factor of $\Delta/2$ to match the order of magnitude of its neighbours.⁴

A better estimate of the effective system size w can be obtained from assigning a segment of length $1/J_i$ to every hopping term (cf. Sec. 2) and scaling the resulting chain to the segment $z \in (-\pi/4, \pi/4)$ that appears in the conformal map (2) (or the circle $\theta \in [0, 2\pi)$ for rings). This yields

$$w_1 = -\log \tan \left(\frac{\pi}{4} \frac{1/J_{\text{middle}}}{\sum_i 1/J_i} \right) \quad (\text{A.1a})$$

$$w_2 = -2 \log \tan \left(\pi \frac{1/J_{\text{middle}}}{\sum_i 1/J_i} \right) \quad (\text{A.1b})$$

for chains and rings, respectively, where J_{middle} is the coupling strength of the bond(s) across the entanglement cut. In the limit $L\Delta \gg 1$, both expressions reduce to

$$w \rightarrow \frac{L\Delta}{2} + f(\Delta); \quad (\text{A.2})$$

the function $f(\Delta)$ can only be obtained analytically for the rainbow chain of Fig. 1(c), where the sums in (A.1) are over geometric series:

$$f_{\text{rainbow}}(\Delta) = -\log \left[\frac{\pi}{8} (e^\Delta - 1) \right]. \quad (\text{A.3})$$

$f(\Delta)$ is tabulated for the values of Δ that appear in the main text in Table 2; convergence to the asymptotic form (A.2) appears to be exponential in $L\Delta$.

⁴As an extreme example, at $\Delta = 0$, all $w_i = 0$, so every site should be mapped onto $z_i = \pm 1$, leading to a zero term in the Hamiltonian across the entanglement cut. Instead, the rainbow-deformed chain construction described in Sec. 2 reduces to a uniform chain.

We can extend the same argument to Hamiltonians with single- and two-site terms, treating both kinds of term as a segment – this is particularly natural for the Majorana representation (8c) of the TFI chain. Eqs. (A.1, A.2) remain applicable, although Δ must be replaced with $\Delta/2$, the effective length of these “segments.”

References

- [1] H. Li and F. D. M. Haldane, *Entanglement spectrum as a generalization of entanglement entropy: Identification of topological order in non-abelian fractional quantum hall effect states*, Phys. Rev. Lett. **101**, 010504 (2008), doi:[10.1103/PhysRevLett.101.010504](https://doi.org/10.1103/PhysRevLett.101.010504).
- [2] F. Pollmann, A. M. Turner, E. Berg and M. Oshikawa, *Entanglement spectrum of a topological phase in one dimension*, Phys. Rev. B **81**, 064439 (2010), doi:[10.1103/PhysRevB.81.064439](https://doi.org/10.1103/PhysRevB.81.064439).
- [3] X. Chen, Z.-C. Gu and X.-G. Wen, *Classification of gapped symmetric phases in one-dimensional spin systems*, Phys. Rev. B **83**, 035107 (2011), doi:[10.1103/PhysRevB.83.035107](https://doi.org/10.1103/PhysRevB.83.035107).
- [4] X.-L. Qi, H. Katsura and A. W. W. Ludwig, *General relationship between the entanglement spectrum and the edge state spectrum of topological quantum states*, Phys. Rev. Lett. **108**, 196402 (2012), doi:[10.1103/PhysRevLett.108.196402](https://doi.org/10.1103/PhysRevLett.108.196402).
- [5] L. Cincio and G. Vidal, *Characterizing topological order by studying the ground states on an infinite cylinder*, Phys. Rev. Lett. **110**, 067208 (2013), doi:[10.1103/PhysRevLett.110.067208](https://doi.org/10.1103/PhysRevLett.110.067208).
- [6] J. I. Cirac, D. Poilblanc, N. Schuch and F. Verstraete, *Entanglement spectrum and boundary theories with projected entangled-pair states*, Phys. Rev. B **83**, 245134 (2011), doi:[10.1103/PhysRevB.83.245134](https://doi.org/10.1103/PhysRevB.83.245134).
- [7] B. Bauer, L. Cincio, B. P. Keller, M. Dolfi, G. Vidal, S. Trebst and A. W. W. Ludwig, *Chiral spin liquid and emergent anyons in a kagome lattice mott insulator*, Nat. Commun. **5**(1), 5137 (2014), doi:[10.1038/ncomms6137](https://doi.org/10.1038/ncomms6137).
- [8] S.-S. Gong, W. Zhu and D. N. Sheng, *Emergent chiral spin liquid: Fractional quantum hall effect in a kagome heisenberg model*, Scientific Reports **4**(1), 1 (2014), doi:[10.1038/srep06317](https://doi.org/10.1038/srep06317).
- [9] A. Szasz, J. Motruk, M. P. Zaletel and J. E. Moore, *Chiral spin liquid phase of the triangular lattice hubbard model: A density matrix renormalization group study*, Phys. Rev. X **10**, 021042 (2020), doi:[10.1103/PhysRevX.10.021042](https://doi.org/10.1103/PhysRevX.10.021042).
- [10] J.-Y. Chen, L. Vanderstraeten, S. Capponi and D. Poilblanc, *Non-abelian chiral spin liquid in a quantum antiferromagnet revealed by an ipeps study*, Phys. Rev. B **98**, 184409 (2018), doi:[10.1103/PhysRevB.98.184409](https://doi.org/10.1103/PhysRevB.98.184409).
- [11] J. Hasik, M. Van Damme, D. Poilblanc and L. Vanderstraeten, *Simulating chiral spin liquids with projected entangled-pair states*, Phys. Rev. Lett. **129**, 177201 (2022), doi:[10.1103/PhysRevLett.129.177201](https://doi.org/10.1103/PhysRevLett.129.177201).
- [12] M. E. Peskin and D. V. Schroeder, *An Introduction to quantum field theory*, Addison-Wesley, Reading, USA, ISBN 978-0-201-50397-5, 978-0-429-50355-9, 978-0-429-49417-8, doi:[10.1201/9780429503559](https://doi.org/10.1201/9780429503559) (1995).

- [13] A. M. Läuchli, *Operator content of real-space entanglement spectra at conformal critical points* (2013), [1303.0741](#).
- [14] J. Cardy and E. Tonni, *Entanglement Hamiltonians in two-dimensional conformal field theory*, *J. Stat. Mech.* **2016**(12), 123103 (2016), doi:[10.1088/1742-5468/2016/12/123103](#).
- [15] Q. Hu, A. Franco-Rubio and G. Vidal, *Emergent universality in critical quantum spin chains: entanglement virasoro algebra* (2020), [2009.11383](#).
- [16] J. L. Cardy, *Boundary conditions, fusion rules and the Verlinde formula*, *Nucl. Phys. B* **324**(3), 581 (1989), doi:[https://doi.org/10.1016/0550-3213\(89\)90521-X](https://doi.org/10.1016/0550-3213(89)90521-X).
- [17] J. Eisert, M. Cramer and M. B. Plenio, *Colloquium: Area laws for the entanglement entropy*, *Rev. Mod. Phys.* **82**, 277 (2010), doi:[10.1103/RevModPhys.82.277](#).
- [18] P. Calabrese and J. Cardy, *Entanglement entropy and conformal field theory*, *J. Phys. A* **42**, 504005 (2009), doi:[10.1088/1751-8113/42/50/504005](#), [0905.4013](#).
- [19] G. Vitagliano, A. Riera and J. I. Latorre, *Volume-law scaling for the entanglement entropy in spin-1/2 chains*, *New J. Phys.* **12**(11), 113049 (2010), doi:[10.1088/1367-2630/12/11/113049](#).
- [20] G. Ramírez, J. Rodríguez-Laguna and G. Sierra, *From conformal to volume law for the entanglement entropy in exponentially deformed critical spin 1/2 chains*, *J. Stat. Mech.* **2014**(10), P10004 (2014), doi:[10.1088/1742-5468/2014/10/P10004](#).
- [21] G. Ramírez, J. Rodríguez-Laguna and G. Sierra, *Entanglement over the rainbow*, *J. Stat. Mech.* **2015**(6), P06002 (2015), doi:[10.1088/1742-5468/2015/06/P06002](#).
- [22] J. Rodríguez-Laguna, J. Dubail, G. Ramírez, P. Calabrese and G. Sierra, *More on the rainbow chain: entanglement, space-time geometry and thermal states*, *J. Phys. A* **50**(16), 164001 (2017), doi:[10.1088/1751-8121/aa6268](#).
- [23] K. G. Wilson, *The renormalization group: Critical phenomena and the Kondo problem*, *Rev. Mod. Phys.* **47**, 773 (1975), doi:[10.1103/RevModPhys.47.773](#).
- [24] R. Bulla, T. A. Costi and T. Pruschke, *Numerical renormalization group method for quantum impurity systems*, *Rev. Mod. Phys.* **80**, 395 (2008), doi:[10.1103/RevModPhys.80.395](#).
- [25] M. B. Hastings, *An area law for one-dimensional quantum systems*, *J. Stat. Mech.* **2007**(08), P08024 (2007), doi:[10.1088/1742-5468/2007/08/P08024](#).
- [26] I. Peschel, *Calculation of reduced density matrices from correlation functions*, *J. Phys. A* **36**(14), L205 (2003), doi:[10.1088/0305-4470/36/14/101](#).
- [27] S. Bravyi, *Lagrangian representation for fermionic linear optics*, *Quant. Inf. Comput.* **5**(3), 216 (2005), doi:[10.26421/QIC5.3-3](#).
- [28] S.-A. Cheong and C. L. Henley, *Many-body density matrices for free fermions*, *Phys. Rev. B* **69**, 075111 (2004), doi:[10.1103/PhysRevB.69.075111](#).
- [29] I. Peschel, *Special review: Entanglement in solvable many-particle models*, *Braz. J. Phys.* **42**(3), 267 (2012), doi:[10.1007/s13538-012-0074-1](#).

- [30] H.-K. Jin, R.-Y. Sun, Y. Zhou and H.-H. Tu, *Matrix product states for Hartree-Fock-Bogoliubov wave functions*, Phys. Rev. B **105**, L081101 (2022), doi:[10.1103/PhysRevB.105.L081101](https://doi.org/10.1103/PhysRevB.105.L081101).
- [31] G. Petrica, B.-X. Zheng, G. K.-L. Chan and B. K. Clark, *Finite and infinite matrix product states for Gutzwiller projected mean-field wave functions*, Phys. Rev. B **103**, 125161 (2021), doi:[10.1103/PhysRevB.103.125161](https://doi.org/10.1103/PhysRevB.103.125161).
- [32] T. Liu, Y.-H. Wu, H.-H. Tu and T. Xiang, *Efficient conversion from fermionic Gaussian states to matrix product states* (2024), [2408.01155](https://arxiv.org/abs/2408.01155).
- [33] S. H. Hille and A. Szabó, In preparation.
- [34] P. Di Francesco, P. Mathieu and D. Senechal, *Conformal Field Theory*, Graduate Texts in Contemporary Physics. Springer-Verlag, New York, ISBN 978-0-387-94785-3, 978-1-4612-7475-9, doi:[10.1007/978-1-4612-2256-9](https://doi.org/10.1007/978-1-4612-2256-9) (1997).
- [35] Y. Liu, H. Shimizu, A. Ueda and M. Oshikawa, *Finite-size corrections to the energy spectra of gapless one-dimensional systems in the presence of boundaries*, SciPost Phys. **17**, 099 (2024), doi:[10.21468/SciPostPhys.17.4.099](https://doi.org/10.21468/SciPostPhys.17.4.099).
- [36] A. Yu. Kitaev, *Unpaired Majorana fermions in quantum wires*, Phys.-Usp. **44**(10S), 131 (2001), doi:[10.1070/1063-7869/44/10S/S29](https://doi.org/10.1070/1063-7869/44/10S/S29).
- [37] R.-Z. Huang, L. Zhang, A. M. Läuchli, J. Haegeman, F. Verstraete and L. Vanderstraeten, *Emergent conformal boundaries from finite-entanglement scaling in matrix product states*, Phys. Rev. Lett. **132**, 086503 (2024), doi:[10.1103/PhysRevLett.132.086503](https://doi.org/10.1103/PhysRevLett.132.086503).
- [38] J. L. Cardy, *Effect of boundary conditions on the operator content of two-dimensional conformally invariant theories*, Nucl. Phys. B **275**, 200 (1986), doi:[10.1016/0550-3213\(86\)90596-1](https://doi.org/10.1016/0550-3213(86)90596-1).
- [39] H. Saberi, A. Weichselbaum and J. von Delft, *Matrix-product-state comparison of the numerical renormalization group and the variational formulation of the density-matrix renormalization group*, Phys. Rev. B **78**, 035124 (2008), doi:[10.1103/PhysRevB.78.035124](https://doi.org/10.1103/PhysRevB.78.035124).
- [40] A. Weichselbaum, *Tensor networks and the numerical renormalization group*, Phys. Rev. B **86**, 245124 (2012), doi:[10.1103/PhysRevB.86.245124](https://doi.org/10.1103/PhysRevB.86.245124).
- [41] J. Hauschild and F. Pollmann, *Efficient numerical simulations with Tensor Networks: Tensor Network Python (TeNPy)*, SciPost Phys. Lect. Notes **5** (2018), doi:[10.21468/SciPostPhysLectNotes.5](https://doi.org/10.21468/SciPostPhysLectNotes.5).
- [42] V. S. Dotsenko, *Critical Behavior and Associated Conformal Algebra of the Z(3) Potts Model*, Nucl. Phys. B **235**, 54 (1984), doi:[10.1016/0550-3213\(84\)90148-2](https://doi.org/10.1016/0550-3213(84)90148-2).
- [43] J. L. Cardy, *Operator content of two-dimensional conformally invariant theories*, Nucl. Phys. B **270**, 186 (1986), doi:[10.1016/0550-3213\(86\)90552-3](https://doi.org/10.1016/0550-3213(86)90552-3).
- [44] G. Mussardo, *Statistical Field Theory*, Oxford Graduate Texts. Oxford University Press, Oxford, ISBN 978-0-19-878810-2 (2020).
- [45] Y. Zhang and A. Vishwanath, *Establishing non-abelian topological order in gutzwiller-projected chern insulators via entanglement entropy and modular S-matrix*, Phys. Rev. B **87**, 161113 (2013), doi:[10.1103/PhysRevB.87.161113](https://doi.org/10.1103/PhysRevB.87.161113).

- [46] Y. Zhang and X.-L. Qi, *Identifying non-abelian topological ordered state and transition by momentum polarization*, Phys. Rev. B **89**, 195144 (2014), doi:[10.1103/PhysRevB.89.195144](https://doi.org/10.1103/PhysRevB.89.195144).
- [47] Y.-H. Wu and H.-H. Tu, *Non-abelian topological order with $SO(5)_1$ chiral edge states*, Phys. Rev. B **106**, 115129 (2022), doi:[10.1103/PhysRevB.106.115129](https://doi.org/10.1103/PhysRevB.106.115129).